

Progress in Visualizing Atomic Size Effects with DFT-Chemical Pressure Analysis: From Isolated Atoms to Trends in AB₅ Intermetallics

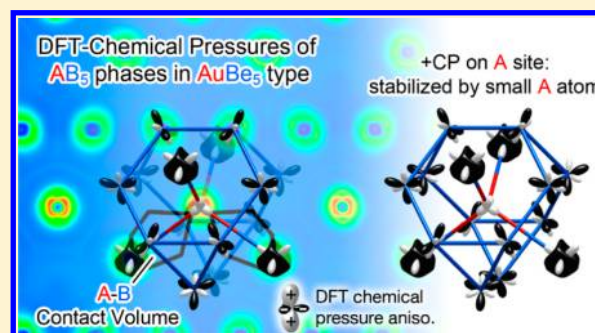
Veronica M. Berns, Joshua Engelkemier, Yiming Guo, Brandon J. Kilduff, and Daniel C. Fredrickson*

Department of Chemistry, University of Wisconsin—Madison, 1101 University Avenue, Madison, Wisconsin 53706, United States

S Supporting Information

ABSTRACT: The notion of atomic size poses an important challenge to chemical theory: empirical evidence has long established that atoms have spatial requirements, which are summarized in tables of covalent, ionic, metallic, and van der Waals radii. Considerations based on these radii play a central role in the design and interpretation of experiments, but few methods are available to directly support arguments based on atomic size using electronic structure methods. Recently, we described an approach to elucidating atomic size effects using theoretical calculations: the DFT-Chemical Pressure analysis, which visualizes the local pressures arising in crystal structures from the interactions of atomic size and electronic effects. Using this approach, a variety of structural phenomena in intermetallic phases have already been understood in terms that provide guidance to new synthetic experiments.

However, the applicability of the DFT-CP method to the broad range of the structures encountered in the solid state is limited by two issues: (1) the difficulty of interpreting the intense pressure features that appear in atomic core regions and (2) the need to divide space among pairs of interacting atoms in a meaningful way. In this article, we describe general solutions to these issues. In addressing the first issue, we explore the CP analysis of a test case in which no core pressures would be expected to arise: isolated atoms in large boxes. Our calculations reveal that intense core pressures do indeed arise in these virtually pressure-less model systems and allow us to trace the issue to the shifts in the voxel positions relative to atomic centers upon expanding and contracting the unit cell. A compensatory grid unwarping procedure is introduced to remedy this artifact. The second issue revolves around the difficulty of interpreting the pressure map in terms of interatomic interactions in a way that respects the size differences of the atoms and avoids artificial geometrical constraints. In approaching this challenge, we have developed a scheme for allocating the grid pressures to contacts inspired by the Hirshfeld charge analysis. Here, each voxel is allocated to the contact between the two atoms whose free atom electron densities show the largest values at that position. In this way, the differing sizes of atoms are naturally included in the division of space without resorting to empirical radii. The use of the improved DFT-CP method is illustrated through analyses of the applicability of radius ratio arguments to Laves phase structures and the structural preferences of AB₅ intermetallics between the CaCu₅ and AuBe₅ structure types.



1. INTRODUCTION

While chemistry has long since stripped itself of the mysticism of the alchemists, its deep roots in experimental observation have led to a number of useful empirical concepts that have their own sort of poetry and allure, such as the chemical bond, electronegativity, and acidity. One goal of modern theoretical chemistry is the mapping of these notions to aspects of a compound's electronic structure, in ways that are both theoretically rigorous yet honor the richness of their historical uses and connotations. Atomic size is perhaps one of the most problematic of these empirical ideas. Experience with molecular and solid state structures suggests that atoms have measurable sizes,^{1–3} yet the Schrödinger equation contains no terms involving atomic radii or explicit penalties for atoms encroaching upon each other. Indeed, the gradual and asymptotic decay of wave functions away from a system's nuclei is far from conducive to the construction of clear-cut boundaries defining the space

occupied by individual atoms.⁴ Given the importance of atomic size arguments throughout chemistry, theoretical tools which overcome these challenges could be extremely beneficial to deepening the roles theory can play in the design of experiments.

For inorganic solid state materials, the need for such theoretical methods for analyzing atomic size effects is particularly pressing, as can be seen in a quick survey of the recent literature. Atomic sizes or radius ratios are frequently invoked in discussions of the factors stabilizing particular crystal structures^{5–16} and in the interpretation of physical properties in terms of the presence of rattling atoms or interstitial spaces for guest atoms.^{17,18} Furthermore, the empirical concept of chemical pressure, in which elemental substitutions create local stresses in a crystal structure, has been used as a framework for

Received: March 22, 2014

Published: June 4, 2014

understanding relationships between composition and properties.^{19–28}

While energy terms corresponding to atomic size effects are difficult to extract from an electronic structure calculation, we have recently found that their impact on stability can be productively inferred from a quantum mechanical adaptation of the chemical pressure concept just mentioned.^{29–32} The basis of this method is the recognition that the size requirements of atoms are most apparent when interatomic repulsion at one contact in a structure impedes bonding at other contacts. As the repulsion and bonding interactions cannot be optimized simultaneously, local stresses are expected to result, which, unlike the atomic sizes themselves, can be evaluated naturally using quantum mechanics through such concepts as the stress density.^{33–38}

The DFT-CP analysis offers a way to examine these local pressures using the results of standard electronic structure calculations. The method uses the density and potential grids determined in the course of a DFT calculation to create maps of the pressure within crystal structures, which reveal points of frustration within those structures. This approach has been particularly fruitful in the study of the structural chemistry of intermetallic phases, where it has offered explanations for such phenomena as the creation of complex structures through the insertion of planar interfaces into simpler ones,^{30,32} the formation of local icosahedral order in quasicrystal approximants,^{39,40} and the ability of some AuCu₃-type lattices to accommodate guest atoms.⁴¹

Over the course of these and other applications, we have found that there are still several issues limiting the range of applicability of the DFT-CP analysis: (1) the proper treatment of the intense pressures that are calculated to occur near the core regions of an atom and (2) the best scheme to interpret the pressure maps in terms of interatomic interactions.

In this article, we will describe improved solutions to both of these challenges. Beginning with the CP calculations on individual atoms isolated in large unit cells, we will show that the introduction of an unwarping procedure to correct for the drift of the voxel positions relative to the nuclei upon expanding and contracting the unit cell can significantly reduce the severe pressures in the atomic core regions obtained in the original procedure. Including this step in the generation of CP-maps allows for more subtle CP features to come to the foreground and reduces the need for our earlier isotropic core averaging technique.

After describing this improved method for the construction of CP maps, we will then move to issues with their interpretation. As the CP distributions generally involve positive pressures near the core regions and negative pressures in the interstitial regions, evaluating the net pressure along a contact involves an averaging process over the voxels associated with that contact. The overall results are strongly tied to the scheme used in assigning these voxels to contacts. In our previous applications, we have found that assuming that a voxel's pressure is determined by the contact between its two closest atoms often provided intuitive results. However, this purely geometrical construction does not always assign differing spheres of influence to atoms of vastly different sizes. In this article, we present a more sophisticated approach inspired by the Hirshfeld method for calculating atomic charges,⁴² in which the electron density distributions of free atoms are used in determining which atoms will have the largest influence on a voxel's pressure.

In introducing these methodological improvements, we will make reference to structural trends in intermetallics that have been attributed to atomic size effects (Figure 1): the role of

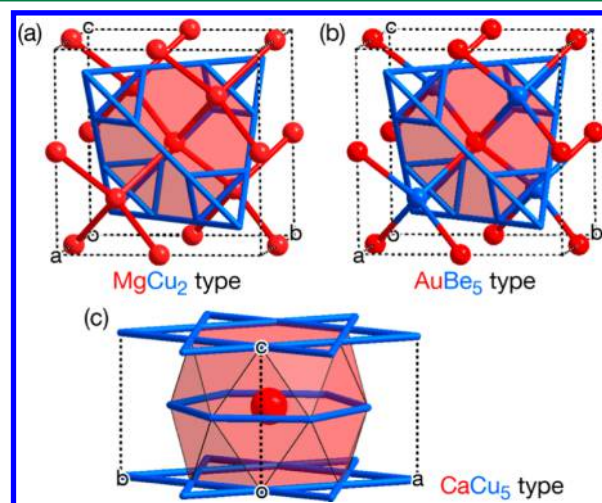


Figure 1. Structure types discussed in this article whose stability ranges are empirically connected to atomic size: (a) The MgCu₂ (cubic Laves phase) type. (b) The AuBe₅ type. (c) The CaCu₅ type.

radius ratios in the Laves phases and the transition from the CaCu₅ type to the AuBe₅ type for AB₅ intermetallics with increasingly smaller A atoms.⁴³ Through the use of the updated DFT-CP method, the latter structural trend will become simply explained as a CP-driven transition in line with the pressure–distance paradox.^{4,44} We anticipate that these results could provide a foundation for analyses of the origins of a series of complex intermetallic phases built from the intergrowth of the AuBe₅ and MgCu₂ types, at compositions near which a CaCu₅-type phase might be expected, such as YbCu_{4.5} with its giant 7448-atom monoclinic unit cell.^{45–48} More generally, the methodological improvements described here should also help make the CP analysis applicable to the full range of chemistry in which atomic size is considered to play a role, from organic molecules to inorganic solids.

2. COMPUTATIONAL PROCEDURES

Electronic structure calculations for the geometrical optimization of crystal structures and the output of electron densities, kinetic energy densities, and components of the Kohn–Sham potentials were carried out with the ABINIT program.^{49,50} All calculations employed the density functional theory (DFT) with the local density approximation (LDA) of Goedecker et al.,⁵¹ and the HGH atomic pseudopotentials.⁵² Further details, including the energy cutoffs, number of k-points used in the calculations, and the optimized atomic coordinates of the intermetallic structures discussed in this article, are given in the Supporting Information.

The output of the ABINIT calculations was used for the generation of CP maps through the scheme described below. The resulting CP maps were visualized with the program VESTA 3.⁵³ The projections of the CP maps onto spherical harmonics were plotted with Matlab. Software for the calculation and integration of CP maps using the method described in this paper is available at our research group Web site (<http://www.chem.wisc.edu/~danny>).

In the determination of Hirshfeld-inspired contact volumes, free atom electron densities were taken either from the ABINIT

Web site or calculated using the Atomic Pseudopotentials Engine.⁵⁴

3. GRID UNWARPING NEAR ATOMIC CENTERS

The basis of the DFT-CP method lies in the ability of the DFT total energy to be at least partially represented as an integral over a spatially resolved energy density:

$$E_{\text{DFT}} = \iiint_{\text{unit cell}} \rho_{\text{energy}}(\vec{r}) dV + E_{\text{remainder}} \quad (1)$$

where $E_{\text{remainder}}$ contains energetic contributions that are not easily traced to specific points in space, such as the Ewald energy and nonlocal components of the potential energy. Using the output of the ABINIT program, such an energy density function can be constructed in the form of discrete points on a grid, i.e.

$$\begin{aligned} E_{\text{DFT}} &\approx \sum_n^{N_{\text{voxels}}} \rho_{\text{energy}}(\vec{r}_n) V_{\text{voxel}} + E_{\text{remainder}} \\ &= \sum_n^{N_{\text{voxels}}} E_n + E_{\text{remainder}} \end{aligned} \quad (2)$$

where N_{voxels} and V_{voxel} are respectively the number of voxels in the structure's unit cell and the volume of each individual voxel.

When we recall that pressure and total energy are related as $P = -\partial E / \partial V$, a straightforward approach to constructing pressure maps emerges. We can simply generate energy grids for a structure at volumes that are slightly contracted and expanded relative to the geometry of interest and use the resulting energy difference at each voxel as the basis for the calculation of voxel pressures:

$$P_n = -\partial E_n / \partial V \quad (3)$$

The representation of the total energy as a sum over an energy grid then gives way to the net pressure experienced by a phase being expressed as the average over a pressure grid:

$$\begin{aligned} P &= -\frac{\partial E_{\text{DFT}}}{\partial V_{\text{cell}}} \\ &= -\sum_n^{N_{\text{voxels}}} \frac{\partial E_n}{N_{\text{voxels}} \partial V_{\text{voxel}}} - \frac{\partial E_{\text{remainder}}}{\partial V_{\text{cell}}} \\ &= \frac{1}{N_{\text{voxels}}} \sum_n^{N_{\text{voxels}}} P_n + P_{\text{remainder}} \end{aligned} \quad (4)$$

where $P_{\text{remainder}}$ is treated as a homogeneous background pressure to be added uniformly to all points of the pressure grid.

In our applications of this procedure, we have found that a rather consistent result is obtained over a wide range of solid state compounds: the pressure maps are marked by intense pressures (of several TPa) near the core regions of the atoms, with much shallower features in the interstitial portions of the structure. The extreme magnitudes of these core pressures mean that success in the interpretation of the pressure map is strongly dependent on how the cores are divided among interatomic interactions.

A key question here is whether the strong pressures in the core regions represent the interactions between atoms or are instead an artifact of the pseudopotential models for the atoms or the procedure for the generation of the pressure maps. A simple way to answer this question is to consider a case in which interatomic interactions should be absent: isolated atoms. In Figure 2a, we show cross-sections of CP maps calculated for individual atoms

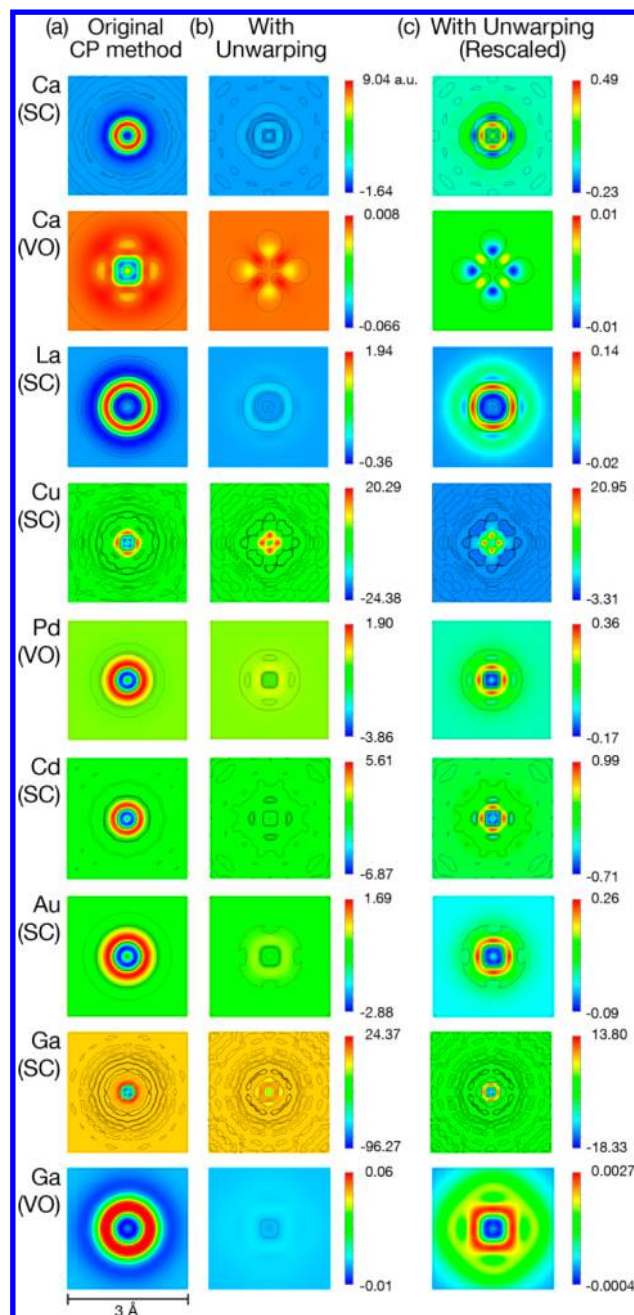


Figure 2. DFT-Chemical Pressure (CP) maps for individual atoms isolated in large unit cells (cell edges of 10 Å). (a) Cross sections through the nuclear positions using the original DFT-CP scheme. (b) The corresponding CP maps calculated using the process for unwarping the energy grids near the atomic cores, plotted using the same color map as in a. (c) The unwarping procedure significantly reduces the strong core-like features around the atomic position (which should be essentially absent in these calculations on virtually isolated atoms). SC and VO refer to the semicore and valence-only versions of the atomic pseudopotentials, respectively, where applicable. Black contours trace isosurface levels at increments of 0.05 between -0.1 and 0.1 au.

placed in large unit cells, for which the interatomic distances are sufficiently long (10 Å) that each atom should exhibit virtually no influence on its neighbors. Maps are shown for a variety of elements, but common features are present: the atomic position at the center of the map is clearly decorated with intense

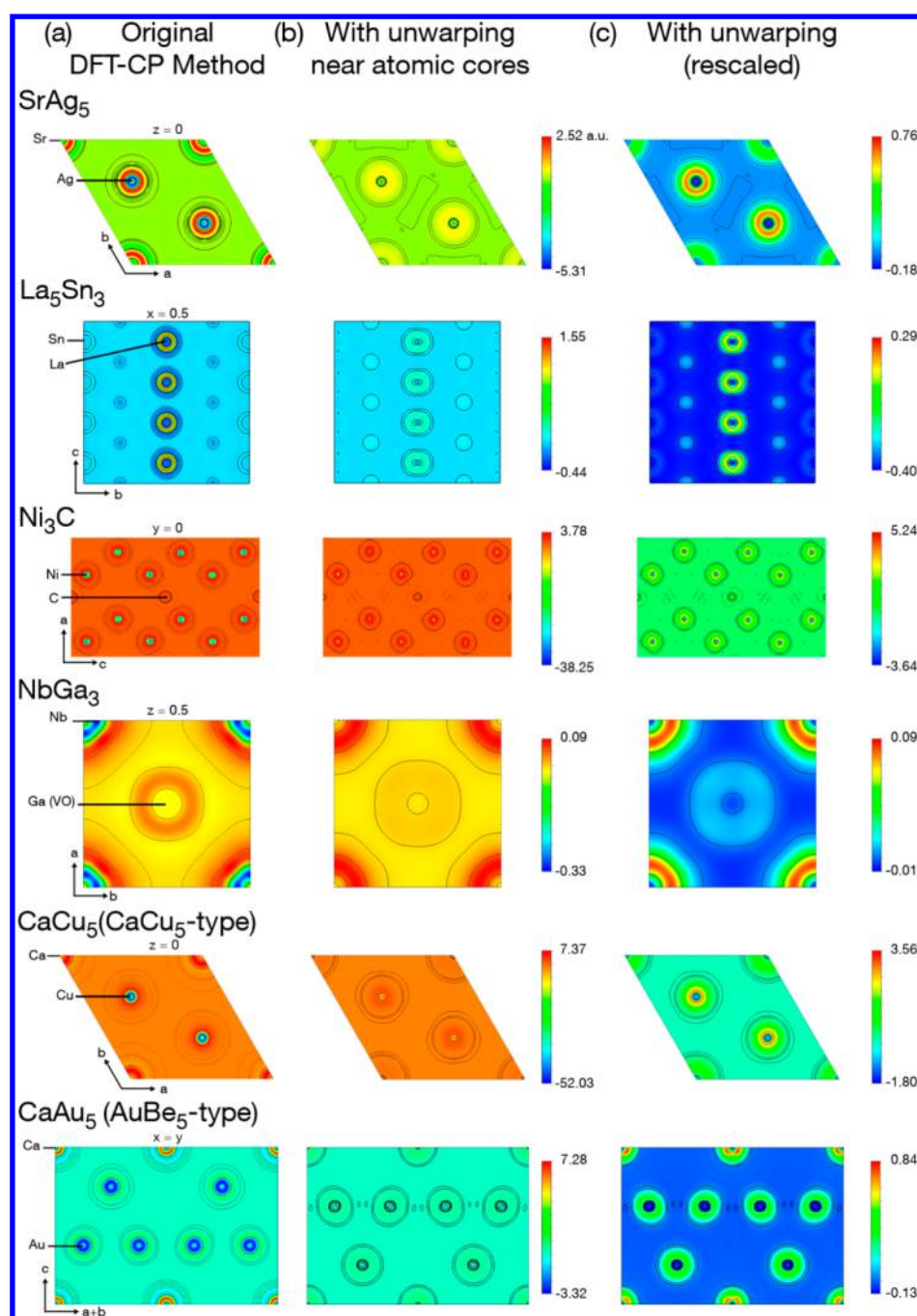


Figure 3. Cross sections for the DFT-CP maps of a variety of intermetallic phases calculated (a) before and (b) after the unwarping of the energy grids using the same color map and (c) the unwarping maps plotted with more appropriately tailored color maps.

oscillating pressure features emanating from the atomic cores. Depending on the diffuseness of the valence electron wave functions, the scales of these features vary over a significant range: from 0.07 atomic units for the valence-only Ca pseudopotential to 120 atomic units for the semicore Ga pseudopotential. In all but the shallowest pseudopotentials, pressures of more than 1 atomic unit are attained. When we recall that 1 atomic unit of pressure is equal to 96 000 GPa, it is apparent that they represent pressure responses that are incommensurately large relative to the minuteness of the perturbations on these systems induced by a small expansion or contraction of the unit cell.

Why should such strong pressures arise in the absence of interatomic interactions? An assumption of the above formulation of the DFT-CP approach is that upon changing a unit cell's volume, the features of the potentials and electron density expand or contract along with the voxel grid.³⁰ In this way, the pressure calculated for a specific voxel (P_n) is then related to the difference in energies calculated for that voxel in slightly expanded and contracted structures:

$$P_n^{\text{DFT-CP}} \approx \frac{E_n^+ - E_n^-}{V_{\text{voxel}}^+ - V_{\text{voxel}}^-} \quad (5)$$

This may be expected to apply well to the regions in the interstitial spaces, where atoms are most responsive to changes in

their surroundings. Near the atomic cores, however, where electrons cling tightly to the nuclei, such an assumption is harder to justify. In the cores, the depths of the atomic pseudopotentials are such that variations in the cell volume would represent only minor changes. The electron density would not be expected to migrate along with an expanded or contracted voxel grid.

It would seem that a more careful consideration is needed for the high electron densities of the core regions. The pressure response at these points in space might be better approximated by assuming that a volume element of fixed size and position relative to the associated atomic core should be sampled for the expanded and contracted structure.

This can be accomplished by supplementing the original DFT-CP methodology with an unwarping procedure. Consider energy density distributions calculated for the equilibrium geometry of a crystal structure, a slightly expanded structure, and a contracted structure, which we can represent respectively as $\rho_{\text{energy}}^0(\vec{r})$, $\rho_{\text{energy}}^+(\vec{r})$, and $\rho_{\text{energy}}^-(\vec{r})$. If we then write the pressure of voxel n in terms of its relationship to its nearby atom j ($\vec{r}_n = \Delta\vec{r}_n^0 + \vec{r}_{\text{atom } j}^0$), then the pressure at that point, assuming that the energy density does not dilate with the voxel grid, can be calculated as

$$P_n \approx - \frac{\{\rho_{\text{energy}}^+(\Delta\vec{r}_n^0 + \vec{r}_{\text{atom } j}^+) - \rho_{\text{energy}}^-(\Delta\vec{r}_n^0 + \vec{r}_{\text{atom } j}^-)\} V_{\text{voxel}}^0}{V_{\text{voxel}}^+ - V_{\text{voxel}}^-} \quad (6)$$

Calculating pressures in this way is complicated by the fact that the energy densities obtained over the course of a CP calculation are expressed in terms of the discrete points of a voxel grid. The vectors $\Delta\vec{r}_n^0 + \vec{r}_{\text{atom } j}^+$ and $\Delta\vec{r}_n^0 + \vec{r}_{\text{atom } j}^-$ then often will lie in between grid points, and the energy densities at those points cannot be determined exactly. Trilinear interpolation, however, can be used to obtain an estimate based on the values for the surrounding voxels. The magnitude of the errors is then related to the fineness of voxel grid spacing relative to the complexity of the electron density function.

This methodology is implemented in our current version of the program *CPmap*. The voxel energies for the expanded and contracted structure are first calculated according to eq 2. The voxels are then associated with specific atomic cores, which can be done by specifying cutoff radii, using a Voronoi scheme,⁵⁵ a more complicated division of space as offered by Bader's QTAIM,⁵⁶ or, as we will describe in more detail below, a Hirshfeld-type weighting.⁴² The voxel centers in the expanded (\vec{r}_n^+) and contracted (\vec{r}_n^-) structures are then shifted to their corresponding positions relative to their atom's nuclear position as in the equilibrium volume structure ($\vec{r}_n = \Delta\vec{r}_n^0 + \vec{r}_{\text{atom } j}^0$). Finally, the pressures at the voxel positions are calculated according to eq 6.

As the shifts in the voxel positions represent a different sampling of the same energy density maps, this interpolation leads to only small changes to the total energy obtained by integrating over the voxel grid (ca. 0.05%). Any small residual pressure resulting from differences in the interpolation error for the expanded and contracted structures is added homogeneously to the pressure map.

In Figure 2b,c, we illustrate the effect of applying this fixed core correction procedure to atoms isolated in boxes. Figure 2b shows cross sections of the pressure maps for the atoms drawn with the same color map as in Figure 2a. The correction leads to a

substantial change in the pressure distribution. The original, strongly oscillating ripples of pressure are now replaced with flatter maps and less isotropic features. Figure 2c focuses on narrower pressure ranges to allow the more subtle features of these maps to be visible. Here, it can be seen that the variations are in many cases more associated with the corners and faces of the unit cell than with the distance to the atomic core.

4. GRID UNWARPING BETWEEN ATOMS

Atoms in more realistic environments should also benefit from this type of core treatment. Figure 3a shows two-dimensional slices of CP maps calculated for a diverse array of intermetallic compounds. For most examples using the original method, the maps show the most intense pressures as nearly perfect circles around the atomic positions. These core regions are set against what appears to be a shallow, nearly homogeneous negative background pressure. As such features are reminiscent of our uncorrected treatment of the atoms-in-boxes of Figure 2a, it seems likely that implementing grid interpolations here should lead to more meaningful CP maps.

For voxels near the cores of any given atom, the path to applying the above procedure is clear: the voxels can be assigned to their nearby atom and then treated according to eq 6. The situation becomes less clear for voxels deeper in the interstitial spaces between the atomic cores, where the energy density features might be expected to migrate to various degrees with the voxel grid as the structure is expanded and contracted. How should the unwarping process be applied to these regions?

A voxel's position in the equilibrium grid can be represented in terms of its placement relative to any of the atoms in the structure:

$$\vec{r}_n = \Delta\vec{r}_{n,\text{atom } 1}^0 + \vec{r}_{\text{atom } 1}^0 = \vec{r}_{n,\text{atom } 2}^0 + \vec{r}_{\text{atom } 2}^0 = \dots \quad (7)$$

As we move to the expanded or contracted volumes, the various atoms will shift to different positions, so that the various equalities of eq 7 cannot be satisfied simultaneously if we keep the $\Delta\vec{r}_{n,\text{atom } j}^0$ vectors constant. Instead, we will need to decide to what degree each of the $\Delta\vec{r}_{n,\text{atom } j}^0$ terms will be weighted in the determination of the \vec{r}_n^+ and \vec{r}_n^- vectors.

One approach to determining these weights can be found in the Hirshfeld method for the extraction of atomic charges from electronic structure calculations.⁴² In the Hirshfeld approach, one begins with a hypothetical case in which the electron density of a compound is simply a superposition of free atom electron densities centered at the nuclear positions of a structure. The relative contributions from these free atom densities at a given point in space is then translated into relative weights for the apportioning of the true electron density between the atoms in the calculation of charges. The free atom electron densities thus serve as a measure of the distance dependence of each atom's influence.

In a similar way, the Hirshfeld method for the atoms surrounding a voxel can be used in assigning weights to each of the equalities in eq 7. We first define a Hirshfeld weight for the influence of atom j on the position of voxel n :

$$w_{j,n} = \frac{\rho_{\text{atom } j}^{\text{FA}}(\vec{r}_n^0)}{\sum_k^{\text{all atoms}} \rho_{\text{atom } k}^{\text{FA}}(\vec{r}_n^0)} \quad (8)$$

where $\rho_{\text{atom } k}^{\text{FA}}(\vec{r}_n^{\text{o}})$ gives the electron density at the position of voxel n calculated for a free atom of the proper element centered at the nuclear coordinates of atom k .

Having defined these weightings, we can then use them in determining how much a voxel should maintain its position relative to each of the atomic centers as the cell is expanded and contracted for the calculation of CP maps:

$$\vec{r}_n^+ = \sum_j^{\text{all atoms}} w_{j,n} (\Delta \vec{r}_{n,j}^{\text{o}} + \vec{r}_{\text{atom } j}^+) \quad (9a)$$

$$\vec{r}_n^- = \sum_j^{\text{all atoms}} w_{j,n} (\Delta \vec{r}_{n,j}^{\text{o}} + \vec{r}_{\text{atom } j}^-) \quad (9b)$$

For voxels near an atomic core, the weight for that atom will dominate these averages, and the original atom-centered interpolation of the previous section is obtained.

In performing this distortion of the voxel grid around the atom centers, the grid points are no longer uniformly distributed, and the voxel volumes become varied throughout the structure. The calculation of the voxel pressures then becomes slightly modified from eq 6:

$$P_n \approx - \frac{\rho_{\text{energy}}^+(\vec{r}_n^+) V_{\text{voxel},n}^+ - \rho_{\text{energy}}^-(\vec{r}_n^-) V_{\text{voxel},n}^-}{V_{\text{voxel}}^+ - V_{\text{voxel}}^-} \quad (10)$$

where the numerator involves the volumes of the specific voxel n in the expanded and contracted structures, and the denominator uses the average voxel volumes for the two structures. A discussion of the determination of the voxel volumes in the distorted grid is provided in the Supporting Information.

Turning on the unwarping procedure (Figure 3b and c) significantly reduces the magnitudes of the pressures of the core regions, allowing more subtle features in the interatomic regions to come more to the foreground. Also, in some cases, particularly La_3Sn_3 and CaAu_5 , the spherical character of the core regions has diminished, making the centers of the atoms appear more responsive to their surroundings. This is more consistent with the philosophy of pseudopotentials which aims to treat explicitly only those electrons that are perceptibly affected by interatomic interactions as part of the valence set.

5. HIRSHFELD-INSPIRED CONTACT VOLUMES

In the previous section, we saw how the features of a CP map could be substantially clarified by introducing a step in which corresponding grid points of the expanded and contracted unit cells are shifted to the same position in space relative to an atom assigned to it. By implementing this procedure, the severe isotropic pressures appearing around the atomic cores are reduced, allowing more subtle features to come to the foreground. Even with this improvement, however, the CP distributions still largely consist of positive regions around the atomic centers that are immersed in a shallower negative background pressure. In examining the overall pressures at particular interatomic contacts, we will then need to examine the net effect of these core-like and interstitial pressures through the integration of the pressure map within domains assigned to individual contacts.

In performing such an integration, the pressure between a pair of atoms will be given by

$$P_{jk}^{\text{contact}} = \sum_n^{N_{\text{voxels}}} w_{jk,n} P_n \quad (11)$$

where $w_{jk,n}$ is the fraction of the pressure at voxel n that is attributed to the interaction between atom j and atom k . The central challenge in carrying out the integrations in a meaningful way is then the determination of the proper weighting scheme, the set of $w_{jk,n}$'s. In our recent applications of the DFT-CP method, we derived our choice of weights from an assumption that a voxel's pressure is determined by the interaction of its two nearest atoms, i.e.

$$w_{jk,n} = \begin{cases} 1, & \text{if atoms } j \text{ and } k \text{ are two closest to voxel } n \\ \frac{1}{m}, & \text{if } m \text{ contacts are tied in above criterion} \\ 0, & \text{if } j \text{ or } k \text{ are not two atoms closest to voxel } n \end{cases} \quad (12)$$

This scheme is advantageous in its simplicity. However, as it is entirely based on geometrical constructions, it neglects the differing ranges of influence of different atom types and should be considered as only a first step toward a more realistic division of space between contacts.

Over the course of our ongoing exploration of intermetallic phases using the DFT-CP method, we have found that for one large and important class of compounds, the Laves phases and their variants, refinements to the weighting scheme are particularly vital. In these AB_2 compounds (see Figure 1a for one example), the A positions (usually occupied by a relatively electropositive element) form a diamond network, a hexagonal diamond network, or an intergrowth of the two. The B atoms occupy the interstitial spaces of the A diamondoid framework and form truncated tetrahedra (TT) around the A atoms. The resulting coordination environment around the A sites is known as a Friauf polyhedron, consisting of a TT of B atoms with A atoms sitting above the hexagonal faces of the TT.

The geometrical features of the Friauf polyhedron make it a challenging test case for the division of space among interatomic contacts. The A–A and A–B distances exhibit a ratio of 1.0445 (for the high symmetry MgCu_2 -type case), with the longer A–A lengths being consistent with the trend that the A sites are generally occupied by the larger atom type. However, using the distance-based criterion described above, the voxels inside the Friauf polyhedron will be assigned to the pairs of atoms to which they are closest. As the A–B interatomic distances are shorter than the A–A ones, these will tend to absorb more voxels, despite the A atoms being larger.

This dominance of the A–B contacts in the voxel assignments has interesting consequences for the integrated CP schemes. In Figure 4a, we show the results for the MgCu_2 -type phase CaPd_2 ,^{57,58} using the projection scheme described previously. Here, the distribution of voxel pressures around each atom is represented by radial surfaces around its nuclear position. The distance of a point on the surface from the nucleus is proportional to the sums of the voxel pressures along that direction, while the color of the surface gives the sign of the pressure. Lobes in black point along directions where the pressure is negative, i.e. contraction would be favorable, while portions of the surfaces in white correspond to positive pressures, where the structure would prefer to expand.

For the Friauf polyhedron of CaPd_2 using the original geometrical construction of contact volumes, the white and

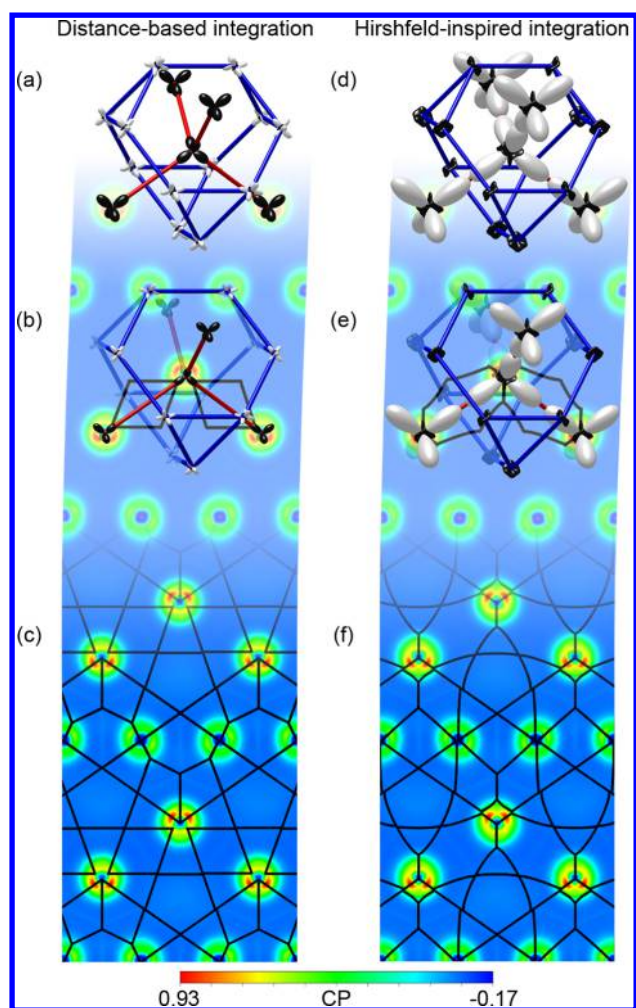


Figure 4. Comparison of integrated DFT-CP anisotropies and contact volumes for CaPd_2 . (a) The DFT-CP distribution calculated for CaPd_2 using the original contact volume (CV) scheme. (b) The DFT-CP distribution plotted together with a cross section of the original DFT-CP map. (c) The DFT-CP cross-section shown separately with the contact volume borders indicated. (d,e) The corresponding images generated using the Hirshfeld-inspired contact volume scheme (see text). In a and d, the pressure distribution around each atom is represented by a radial plot, with the radial distance indicating the magnitude of the sum of voxel pressures along that direction. The sign of the pressure is indicated with color: black for negative (evoking the image of a black hole acting on the structure), white for positive.

black features are divided largely by element type. The Ca atoms appear as black tetrapods, with large negative pressure lobes pointing along the Ca–Ca contacts (red). These forces calling for the contraction of the lattice are counteracted by white, positive pressure lobes along the Pd–Pd contacts (blue), with the Ca–Pd contacts appearing to be relatively satisfied. This result is encouraging in the sense that the heteroatomic interactions, the usual driving force for the formation of a binary phase from its elements, are well-optimized.

However, inspection of the contact distances uncovers some counterintuitive aspects of this picture. Note that in the Ca–Ca/Pd–Ca distance ratio of 1.0445, the Ca–Ca contacts are only slightly longer than the Ca–Pd ones, despite the metallic radius of Ca being significantly larger than that of Pd (1.97 vs 1.37 Å⁵⁹). As a consequence, the Ca–Ca distance is much shorter than the sum of the metallic radii (3.32⁵⁷ vs 3.94 Å⁵⁹). This distance is still

within the ranges observed for Ca–Ca interactions in the Inorganic Crystal Structure Database^{60,61} but would hardly be the occasion for large negative pressures demanding even closer Ca–Ca contacts. If anything, a positive pressure pushing toward distances more in line with twice the metallic radius would be expected.

A look at the volumes assigned to each contact in our integration provides an explanation for the appearance of these negative Ca–Ca pressures. In Figure 4b,c, we present a cross section of the DFT-CP map for CaPd_2 taken through one of the Ca–Ca contacts, with the boundaries between contact volumes drawn in black. The contact volume of the Ca–Ca interaction appears here as a diamond between the two atoms. A brief glance reveals why negative pressures are assigned to this contact: whereas positive pressure features occur around both the Ca atoms of the contact, only the tips of the narrow corners of the contact volume reach into these regions. Instead, the contact volume contains mainly the negative pressure interstitial space between the Ca atoms. The core regions themselves are dominated by Ca–Pd contact volumes.

In other words, the Ca–Pd distances are short enough relative to the Ca–Ca ones that the distance criterion grants them most of the Ca core voxels. As a result, only small positive pressure components are allocated to the Ca–Ca contacts, and negative pressures thus dominate despite the short Ca–Ca distances.

Now that we see the origin of the Ca–Ca negative pressures, a way to correct the CP picture becomes apparent: the Ca–Ca contact volumes should be expanded into the Ca core regions to better reflect the larger size of the Ca atoms relative to Pd atoms. To do this, a change in the weighting scheme of eq 12 is needed that takes into account the differing electronic structures of Ca and Pd atoms.

As for our grid-interpolation scheme above, the Hirshfeld approach can be adapted to this task, the essential change being that we are now assigning points in space to pairs of atoms rather than individual atoms. The influence of a contact on a point in space will depend on the sizes of the free atom electron densities for the two atoms at that point. A way of quantifying this is to consider the weights in eq 11 as being proportional to the products of the free atom (FA) electron densities for the atoms of the contact:

$$w_{jk,n} \propto \rho_{\text{atom } j}^{\text{FA}}(\vec{r}_n) \cdot \rho_{\text{atom } k}^{\text{FA}}(\vec{r}_n) \quad (13)$$

In this way, every voxel would be shared among multiple contacts, with weights that are proportional to the overlaps between the FA electron densities for each contact.

In experimenting with such integration schemes, we have found that following through with this Hirshfeld-based approach in its entirety leads to some issues with interpretation: it is difficult to see which points in space are influencing which contacts. Instead, it is more practical to keep the division of space into discrete contact volumes as in eq 12, but using the products of FA electron densities as a guide to their construction. The corresponding weighting is then:

$$w_{jk,n} = \left\{ \begin{array}{l} 1, \text{ if } \rho_{\text{atom } 1}^{\text{FA}}(\vec{r}_n) \rho_{\text{atom } 2}^{\text{FA}}(\vec{r}_n) \text{ is largest for } j, k \text{ pair} \\ \frac{1}{m}, \text{ if } m \text{ contacts are tied in above criterion} \\ 0, \text{ if } \rho_{\text{atom } 1}^{\text{FA}}(\vec{r}_n) \rho_{\text{atom } 2}^{\text{FA}}(\vec{r}_n) \text{ not largest for } j, k \\ \text{pair} \end{array} \right\} \quad (14)$$

The result of using this Hirshfeld-inspired scheme is shown in Figure 4d,e. The Ca–Ca contact volume (Figure 4e) now reaches much deeper into the Ca cores so that a corner lies on each Ca nuclear position. The angle at each of these corners has also expanded to encompass more of the core's volume. In fact, the core is now entirely divided between the four Ca–Ca contacts arranged in a tetrahedron around the central Ca atom.

At first glance, the new contact volume boundaries do not appear to align with the prominent features of the Ca core regions. In the cross-section of Figure 4f, each Ca atom exhibits a pair of red bulges corresponding to high positive pressures. Their directional character would lead us to think that they are associated with particular interatomic interactions. However, they are almost perfectly bisected by the borders of the CVs, rather than being centered within a specific CV. A deeper investigation of these features resolves this apparent discrepancy. As illustrated in the Supporting Information, we have found that the highest pressures within the core regions tend to accumulate in the spaces lying between important interatomic interactions, rather than along them. The source of this is a negative pressure contribution arising from the overlap of the local pseudopotentials along the interatomic vector. The core regions not aligned with these vectors then tend to be the spaces where the positive core pressures are most prominent.

The increased contribution from the Ca cores to the Ca–Ca contact volumes has a profound effect on the integrated CP distributions (Figure 4d). The Ca–Ca contacts now exhibit intense positive pressures that seem appropriate to the relatively short Ca–Ca distances. These positive pressures are balanced by the negative pressure lobes oriented along the Ca–Pd interactions. The Pd–Pd contacts, meanwhile, are largely devoid of CP features, indicating that the distances here are nearly optimal.

In comparing Figure 4a and d, it is somewhat surprising that they represent the same original CP map and differ only in the integration scheme used. In what ways are they connected? To see their relationship to each other, it is helpful to note that the Ca–Ca contacts pass through hexagons of Pd atoms. The integrated pressures in this region of the structure will depend on the relative sizes and shapes of Ca–Ca, Ca–Pd, and Pd–Pd contact volumes. In the original scheme, the size of the Pd atoms is overestimated relative to the Ca ones, which leads to the Ca–Pd and Pd–Pd volumes dominating the positive cores of the Ca and Pd atoms. The result is positive pressures along the Pd–Pd interactions and only small negative pressures along the Ca–Pd ones.

In moving to the Hirshfeld-inspired scheme, the Ca–Ca volumes are increased at the expense of the Ca–Pd and Pd–Pd volumes. The contact volumes involving Ca then pick up more of the positive core pressures, leading to large positive pressures between the Ca atoms, the removal of positive pressures from the Pd–Pd interactions, and only smaller changes to the Ca–Pd interactions (which lose core contributions from the Ca but gain them from the Pd).

The better treatment of atomic sizes is not the only reason for which the revised CP scheme is attractive: it also corresponds closely with expectations based on the classic sphere-packing view of the Laves phases. Consider a MgCu₂-type AB₂ structure constructed from hard spheres with radius r_A for the A atoms and r_B for the B atoms. The high symmetry of the structure means that the distances are entirely determined by the length of the cubic unit cell edge, and no other degrees of freedom exist for adjusting the structure to accommodate the values of r_A and r_B . If the B atoms are in contact with each other at an interatomic distance of $2r_B$, then the surfaces of the A atoms touch each other when the r_A/r_B radius ratio is $(3/2)^{1/2} = 1.225$. However, the surfaces of the A atoms would not touch those of the B atoms until $r_A/r_B = (11/2)^{1/2} - 1 = 1.345$. As such, bringing the A and B spheres in contact would require allowing the A atoms to slightly interpenetrate each other.

We can now compare these radius ratios to that of the metallic radii for CaPd₂, $r_{\text{Ca}}/r_{\text{Pd}} = 1.97 \text{ \AA}/1.37 \text{ \AA} = 1.44$. For this ratio, having sphere surfaces touch at the Pd–Pd or Ca–Pd contacts would require the Ca spheres to overlap. In this situation, positive pressures could be expected to arise between the Ca atoms as the structure strives to achieve closer contacts along the Pd–Pd and Ca–Pd interactions. This picture agrees well with the CP scheme of Figure 4d–f. It also resonates strongly with W. B. Pearson's prescient analysis of sphere compression in the Laves phases based on geometrical arguments.⁶² In fact, the large positive Ca–Ca CP features in Figure 4d are anticipated by Pearson's plot of A atom compression as a function of radius ratio.

We anticipate that the revised CP scheme obtainable for Laves phases will offer opportunities to examine the driving forces for the creation of complex structures through the fragmentation of these simpler structures^{63–71} and will improve our ability to discern the reasons for the intergrowth of Ca–Cd and Cd–Cu interactions in the Bergman-type quasicrystal approximant Ca₁₀Cu₂Cd₂₇.³⁹

It is important to mention, however, that this result is dependent on the use of a semicore Ca pseudopotential in which not only the Ca 4s but also 3p and 3s electrons are considered as part of the valence set. Using a "valence-only" Ca pseudopotential with just the 4s electrons treated explicitly leads to a CP scheme similar to Figure 4a regardless of what map generation and integration procedures are applied. We believe that this can be attributed to the relatively high ionicity expected for the CaPd₂ phase. Indeed a Bader charge analysis using the *BADER* program^{72–74} of our valence-only electron density for this phase gives a charge on the Ca atoms of +1.7, indicating that only 0.3 electrons lie near the Ca cores. With so few valence electrons present on Ca atoms, it is understandable that the explicit inclusion of semicore electrons would be necessary to model the atom's responses to its surroundings. From this, we arrive at a recommendation that semicore potentials be used in cases where atoms are expected to be highly cationic.

Using the improved method including Hirshfeld-inspired contact volumes and interpolation within atomic cells, we have also been able to reproduce the conclusions of our earlier studies examining the stability of the complex Ca₂Ag₇ and Ca₃₆Sn₂₃ structures relative to simpler structural alternatives. In the remainder of this article, we will describe a different application of the DFT-CP method: determining the role of atomic size in the relative stabilities of competing structure types. Our focus will be on the structural preferences of AB₅ structures for CaCu₅- or

AuBe₅-type structures, for which atomic size has been considered a key factor.

6. STABILITY TRENDS IN AB₅ INTERMETALLICS

In the previous sections of this paper, we described improvements to the DFT-CP method and showed how they offer a CP scheme for the Laves phase CaPd₂ that is in close accord with radius ratio considerations. Using the same implementation of the CP concept, it is also possible to explain the stability trends for another intermetallic structure type that is closely related to the Laves phases: the AuBe₅ type. This AB₅ structure type can be derived from the AB₂ MgCu₂-type by replacing every other A atom in the structure with a B atom, i.e., A₂B₄ → ABB₄ = AB₅ (Figure 1b). For AB₅ intermetallics with A being an alkaline earth or lanthanide and B being a late transition metal, the AuBe₅ type is in competition with the more common CaCu₅ type. The factor determining the relative stabilities of these two structure types appears to be the relative sizes of A and B atoms,⁴³ an effect that should be amenable to CP analysis.

Let us begin by examining the DFT-CP distribution for a representative of the AuBe₅ type: CaAu₅.⁷⁵ In Figure 5, we

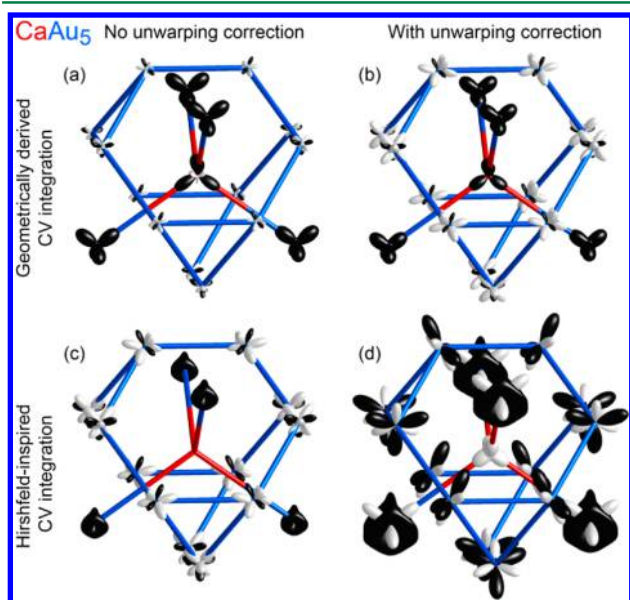


Figure 5. Comparison of DFT-CP anisotropy schemes calculated for CaAu₅ using (a) the original methodology, (b) the improved map generation (with the unwarping procedure applied) but original geometrically constructed contact volumes, (c) the original map generation but the Hirshfeld-inspired contact volume determination, and (d) the improved methods for the both the creation of maps and contact volumes. See the caption to Figure 4 for plotting contentions.

present CP anisotropy surfaces for this structure calculated with the range of procedures discussed in the previous section. First, in Figure 5a, we show the result using the original methodology without grid unwarping and using a geometrical construction for the contact volumes. In Figure 5b,c, we turn on either the unwarping procedure or the Hirshfeld-inspired determination of contact volumes (CVs). Finally, in Figure 5d, we use the fully improved method, with both the unwarping and new contact volumes.

Using the original DFT-CP scheme, the integrated CP distribution closely resembles that obtained in this way for the Laves phase CaPd₂ (Figure 4a), despite having replaced four Ca–Ca contacts with Ca–transition metal ones. Negative

pressure lobes (black) point through the faces of the truncated tetrahedron just as in CaPd₂, while the edges of the truncated tetrahedron itself are decorated with positive pressure lobes. The Ca atom, overall, has large negative pressure indicating that it would benefit from contraction of the lattice, which is prevented by positive pressures within the Au truncated tetrahedra. As such, this scheme predicts that the structure would be stabilized by replacing the Ca with a larger atom—which of course runs counter to the empirical trend of the AuBe₅ type being observed for small A atoms.

Turning on either the interpolation near atomic cores (Figure 5b) or the Hirshfeld-inspired CVs (Figure 5c) introduces qualitative changes to the CP distributions on the Ca@Au₄ tetrahedron but leaves the positive pressures between the Au atoms of the truncated tetrahedron largely intact. The most dramatic change occurs upon turning on both features of the improved DFT-CP method simultaneously (Figure 5d). Here, positive CP lobes point along all of the Ca–Au contacts, while negative CP is reserved for the Au–Au interactions with the longest interatomic distances.

Unlike that of the original DFT-CP scheme, the final integrated result is in close agreement with experimental trends: the positive pressures surrounding the Ca atoms indicate that the stability of this structure will be largely dependent on having a relatively small atom at this position.

In comparing Figures 5b and d, it is evident that the use of Hirshfeld-inspired CVs plays a significant role in obtaining positive pressures on the Ca sites. As for CaPd₂, a comparison of the CVs generated with the original and Hirshfeld-inspired schemes is helpful in seeing how these differences arise (Figure 6). On moving from the MgCu₂ type to the AuBe₅ type, the relative interatomic distances are left unchanged. Because of this, the Ca–Ca geometrically derived CV in CaPd₂ (Figure 4b) is identical to the corresponding one in CaAu₅ (Figure 6b), although now it corresponds to a Ca–Au CV. In the slice through the structure of Figure 6, this CV appears as a diamond-shaped polygon. Only the narrow corners of this polygon cross into the positive core regions of the Ca and Au atoms, leading to a net negative pressure for the contact.

As we switch to the Hirshfeld-inspired scheme, the larger size of the Ca atoms relative to Au will lead to the growth of the Ca–Au CVs at the expense of the Au–Au ones. Because the Ca is surrounded by Au atoms, the shapes of the CVs near the Ca center are essentially unchanged. However, on the Au atoms, there is a marked expansion of the Ca–Au CVs into regions previously occupied by Au–Au ones (Figures 6c,f). The Au–Ca CVs then acquire more of the positive core pressures on the Au atoms, leading to the overall positive CPs between the Ca atom and its neighbors.

As we mentioned earlier, the positive pressures calculated for the Ca atom with the revised CP scheme (Figure 5d) suggest that the AuBe₅ type would be stabilized by the replacement of relatively small atoms on this site. Whether a AuBe₅ phase forms, however, is not just a factor of the favorability of that single phase but will depend also on the free energy of the AuBe₅-type compound relative to those with alternative structures (or multiphase mixtures of compounds with an average A/B ratio of 1:5). For AB₅ intermetallics formed between an electropositive metal such as an alkaline earth or lanthanide (for the A sites) and a late transition metal (for the B sites), the AuBe₅ type has a fierce competitor: the CaCu₅ type (Figure 1c). What does the improved DFT-CP approach predict about the relative virtues of these two structure types?

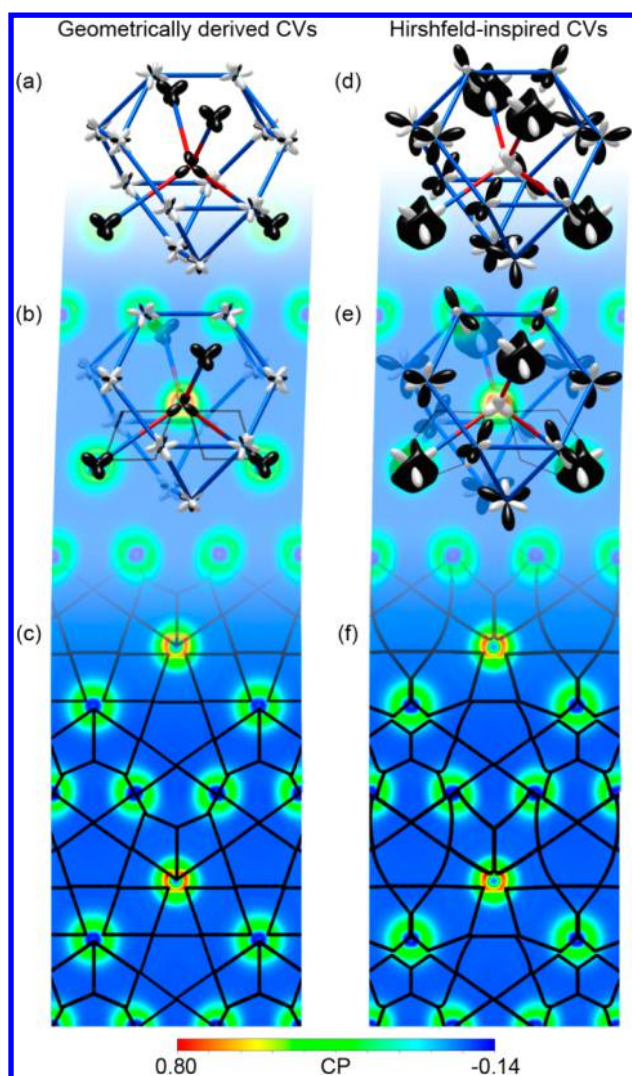


Figure 6. Effect of the use of Hirshfeld-inspired contact volumes (CVs) on the integrated DFT-CP results for CaAu_5 (AuBe_5 type). (a) Atomic DFT-CP anisotropy surfaces calculated for CaAu_5 using the original geometrical definition of CVs. (b) The DFT-CP anisotropy surfaces drawn in the context of a cross section of the DFT-CP map with two Ca–Au CVs in the original scheme indicated. (c) The same cross section of the CP map as in b with additional CV borders drawn. (d–f) The corresponding plots obtained using the Hirshfeld-inspired CV scheme. Note that the CV borders are determined only to the resolution of voxel grid used in the CP calculation. The smooth curves drawn should thus be considered as approximate. See the caption to Figure 4 for an explanation of plotting conventions for the DFT-CP anisotropies.

In Figure 7, we present a comparison of the CP schemes calculated for the CaCu_5 - and AuBe_5 -type structures for two different compounds: CaCu_5 and CaAu_5 , which are experimentally known to prefer the former and latter structure type, respectively (green boxes).^{75,76} The plots shown focus on the coordination environment of the Ca atoms (A site) as the relative size of the atom here has been perceived as a key factor in determining which structure type is adopted. In the CaCu_5 -type structures, this Ca environment consists of an 18-coordinate hexagonal polyhedron built from the layering of honeycomb and kagome sheets of Cu/Au atoms. For the AuBe_5 -type structures, the Ca coordination environment is the same Friauf polyhedron of Cu/Au atoms that we saw earlier in Figures 5 and 6.

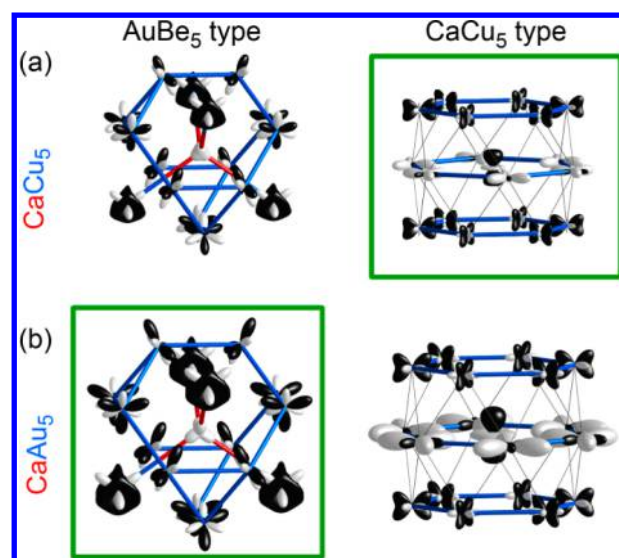


Figure 7. DFT-CP analysis of the AB_5 structure types CaCu_5 and AuBe_5 . (a) CaCu_5 in the AuBe_5 and CaCu_5 types. (b) CaAu_5 in the same two structure types. Plotting conventions are given in the caption to Figure 4.

A comparison of the results for CaCu_5 and CaAu_5 reveals that, while differences occur in the sizes of the various lobes, the qualitative features of the CP plots are very similar between the phases of the same structure types. For both CaCu_5 -type compounds, the Ca atom's CP surface has the shape of a d_{z^2} orbital, with negative lobes pointing up and down and a torus of positive pressure running around the middle. This shape can be interpreted as the Ca atom desiring shorter contacts to the Cu/Au atoms in the layers above and below it but longer contacts to those in the same plane. Overall, the pressures on the Ca sites are negative (-389 GPa on CaCu_5 and -21 in CaAu_5), indicating that the combined effect of the 12 overly long contacts to the Cu/Au atoms above and below outweighs the six overly short contacts in the plane. The net negative CP for the Ca could be relieved by the placement of a larger atom on this site, leading to the prediction that the stability of the phase is enhanced for larger A atoms.

In both of the AuBe_5 -type phases, on the other hand, the Ca sites are subject to positive pressures, indicative of a desire for the expansion of the lattice. This driving force of enlarging the unit cell is resisted largely by the presence of negative pressure lobes between the Cu/Au atoms of the truncated tetrahedron and the Cu/Au atoms on the diamondoid network, which like the Ca atoms lie in Friauf polyhedra. Due to the symmetry of the structure, the interatomic distances between the atoms in the Friauf polyhedra and their surroundings are the same, regardless of whether the position is occupied by a Ca atom or a Cu/Au one. As such, the structure would be best served by placing an atom on the Ca site with a size more similar to a Cu/Au atom, i.e. a smaller atom.

From these considerations, we can conclude that the CaCu_5 and AuBe_5 structure types are indeed tailored for a larger and smaller atom on the A atom positions, respectively. Let us now examine how the CP results for the experimentally observed phases compare with the hypothetical ones. As a first step, we need to calibrate ourselves in terms of the significance of the sizes of the CP features in Figure 7. The CP lobes for the two CaCu_5 phases in panel a are drawn to scale, as are the two CaAu_5 phases in panel b. Between the panels a and b, it is not practical to show the plots at the same scale: Cu with its highly localized 3d

electrons generally shows inherently larger pressures numerically than Au, regardless of the structure. Instead, panels a and b are scaled so that the relative features of the CaCu_5 - and AuBe_5 -type structures are maximally comparable.

A good place to begin is a comparison of the two AuBe_5 -type phases. As we noted earlier, the CP features are very similar between CaCu_5 and CaAu_5 in this structure type. However, a close examination of the Ca CP anisotropy surfaces for the two compounds reveals an important difference: in CaAu_5 , the positive pressures around the Ca are largely focused along the diamondoid network. The contacts between the Ca and the truncated tetrahedron are more satisfied. Upon replacing the Au atoms with smaller Cu ones to create a AuBe_5 -type CaCu_5 phase, we obtain a different situation. The smaller size of Cu translates into a larger relative size for the Ca, and now the positive pressures around the Ca are more uniformly distributed.

By contrast, the replacement for Au with the smaller Cu atoms to make the CaCu_5 -type CaCu_5 phase leads to a tighter coordination environment around the Ca. As a result, the size of the Ca CP features decreases in the CaCu_5 type during this substitution, relative to those of the AuBe_5 -type phase of the same composition.

These observations are in-line with the trend that moving from CaAu_5 to CaCu_5 increases the favorability of the CaCu_5 type relative to the AuBe_5 type. What is more difficult to determine is where the crossing point between the two structure types should occur. This difficulty, in fact, reflects one of the limitations of the use of the DFT-CP method in comparing very different crystal structures. Chemical pressures represent derivatives of the total energy with respect to structural perturbations, and not the magnitudes of the total energy itself. For structures that are closely related, such as a superstructure and the basic structure that it is derived from, the CPs are charting similar energy vs distance curves for interatomic interactions. As such, minimizing the CPs can be seen as a qualitative surrogate for the minimization of the total energy. For more distantly related structures, such as the CaCu_5 and AuBe_5 types, the energy vs distance relationships may be expected to be quite different. We should then seek complementary methods, such as the crystal orbital Hamilton population,⁷⁷ to measure the magnitudes of the bond strengths to go along with the derivatives provided by the DFT-CP analysis.

7. CONCLUSIONS

The concept of chemical pressure offers a means to track the effects of atomic size on the electronic structure of a compound. In this article, we have described advances in the generation of chemical pressure maps for solid state structures using the output of DFT calculations and the interpretation of these maps in terms of interatomic interactions. For the calculation of CP maps, we introduced a correction for the incompressibility of atomic cores in which voxel positions between structures of different sizes are interpolated to the same position relative to the atom with which they are associated. The result is the large reduction of the isotropic core pressures (by factors of up to 15) that have proven so challenging to analyze in previous applications of the DFT-CP approach.

We also introduced an improved scheme for assigning voxels to interatomic contacts for the integration of interatomic pressures: the use of Hirshfeld-inspired contact volumes. In this approach, the relative sizes of the free atom electron densities centered at the atomic positions within a crystal structure are used to evaluate their relative degrees of influence on the

pressure at a given voxel. The voxel is then assigned to the interaction between the pair of atoms whose influence is greatest on it. Through the use of the free atom electron density profiles, the differing size of the atoms becomes naturally incorporated into the construction of contact volumes, unlike our earlier geometrical procedure. This formalism is also easily generalized: the radial electron density of the free atom could easily be replaced in the input to the CP programs with other relevant profile functions, such as the local energy component of the atomic pseudopotentials.

The utility of the improved DFT-CP approach was illustrated using several structures whose stability ranges have been associated with atomic size effects: the MgCu_2 (cubic Laves phase), AuBe_5 , and CaCu_5 structure types. For the MgCu_2 -type CaPd_2 , the CP scheme obtained exhibited parallel features with the sphere-packing view of the Laves phases and thus affirms the efforts of several researchers to apply and adapt radius ratio type analyses to this large family of compounds.^{2,62,78,79} In the case of competition between the AuBe_5 and CaCu_5 types for AB_5 structures, our analyses confirmed the role of atomic size in stabilizing one phase over the other. A moderately sized A atom is predicted to experience positive pressures in the AuBe_5 type and negative pressures in the CaCu_5 type. Relatively large A atoms are then expected to prefer the CaCu_5 -type, while smaller A atoms would prefer the AuBe_5 type.

We have already found that these advances in the DFT-CP method have made its use much more straightforward for a wide variety of intermetallic systems and are looking forward to exploring its capabilities through further applications. Motivated by the insights the method has provided regarding the factors influencing the stabilities of the Laves phases and the AB_5 structure types, we are particularly excited to see what it might reveal concerning the complex intergrowth structures of the AuBe_5 and MgCu_2 structure types in lanthanide-copper systems, some with thousands of atoms per unit cell.^{45–48}

While our specific applications have focused on intermetallic phases, the DFT-CP approach is by no means limited to these systems. As this analysis simply represents a way of converting DFT results into pressure grids, it should be applicable to any compound for which a crystal structure is known (or can be proposed), and for which DFT is considered an adequate treatment. We are looking forward to seeing to what degree this method can elucidate the stresses caused by size effects beyond inorganic solid state compounds, particularly in molecular systems.

■ ASSOCIATED CONTENT

Supporting Information

Detailed computational procedures, optimized atomic coordinates and total energies of the intermetallic crystal structures discussed, discussion of directionality of pressure features near atomic cores, and procedure for the calculation of voxel volumes in distorted grids. This material is available free of charge via the Internet at <http://pubs.acs.org>.

■ AUTHOR INFORMATION

Corresponding Author

*E-mail: danny@chem.wisc.edu.

Notes

The authors declare no competing financial interest.

■ ACKNOWLEDGMENTS

We gratefully acknowledge the financial support of the National Science Foundation through grant DMR-1207409. This research involved calculations using computer resources supported by National Science Foundation Grant CHE-0840494.

■ REFERENCES

- (1) Bondi, A. J. *Phys. Chem.* **1964**, *68*, 441–451.
- (2) Simon, A. *Angew. Chem., Int. Ed.* **1983**, *22*, 95–113.
- (3) van der Waals, J. D. In *Nobel lectures, including presentation speeches and laureates' biographies*; Elsevier Publishing Company: New York, 1967; pp 254–265.
- (4) Müller, U. *Inorganic structural chemistry*; 2nd ed.; Wiley: Chichester, England, 2007; pp 45–50.
- (5) Levy, O.; Jahnátek, M.; Chepulska, R. V.; Hart, G. L. W.; Curtarolo, S. J. *Am. Chem. Soc.* **2010**, *133*, 158–163.
- (6) Wang, H.; Wang, F.; Jones, K.; Miller, G. J. *Inorg. Chem.* **2011**, *50*, 12714–12723.
- (7) Wendorff, M.; Röhr, C. Z. *Anorg. Allg. Chem.* **2011**, *637*, 1013–1023.
- (8) Deringer, V. L.; Goerens, C.; Esters, M.; Dronskowski, R.; Fokwa, B. P. T. *Inorg. Chem.* **2012**, *51*, S677–S685.
- (9) Lin, Q.; Smetana, V.; Miller, G. J.; Corbett, J. D. *Inorg. Chem.* **2012**, *51*, 8882–8889.
- (10) Osters, O.; Nilges, T.; Schöneich, M.; Schmidt, P.; Rothballer, J.; Pielhofer, F.; Wehrich, R. *Inorg. Chem.* **2012**, *51*, 8119–8127.
- (11) Samal, S. L.; Lin, Q.; Corbett, J. D. *Inorg. Chem.* **2012**, *51*, 9395–9402.
- (12) Smetana, V.; Miller, G. J.; Corbett, J. D. *Inorg. Chem.* **2012**, *51*, 7711–7721.
- (13) Crivello, J.-C.; Breidi, A.; Joubert, J.-M. *Inorg. Chem.* **2013**, *52*, 3674–3686.
- (14) Khatun, M.; Stoyko, S. S.; Mar, A. *Inorg. Chem.* **2013**, *52*, 3148–3158.
- (15) Samal, S. L.; Gulo, F.; Corbett, J. D. *Inorg. Chem.* **2013**, *52*, 2697–2704.
- (16) Pöttgen, R. Z. *Anorg. Allg. Chem.* **2014**, *640*, 869–891.
- (17) Emami, H.; Souques, R.; Crivello, J.-C.; Cuevas, F. J. *Solid State Chem.* **2013**, *198*, 475–484.
- (18) Shoko, E.; Kearley, G. J.; Peterson, V. K.; Mutka, H.; Koza, M. M.; Yamaura, J.-i.; Hiroi, Z.; Thorogood, G. J. *arXiv ePrints* **2013**, arXiv:1310.8137 [cond-mat.mtrl-sci].
- (19) Yzambart, G.; Belle, N.; Nasser, G.; Jeannin, O.; Roisnel, T.; Fourmigué, M.; Auban-Senzier, P.; Íñiguez, J.; Canadell, E.; Lorcy, D. J. *Am. Chem. Soc.* **2012**, *134*, 17138–17148.
- (20) Sung, N. H.; Roh, C. J.; Kang, B. Y.; Cho, B. K. *J. Appl. Phys.* **2012**, *111*, 07E117.
- (21) Huang, W.-Y.; Yoshimura, F.; Ueda, K.; Shimomura, Y.; Sheu, H.-S.; Chan, T.-S.; Chiang, C.-Y.; Zhou, W.; Liu, R.-S. *Chem. Mater.* **2014**, *26*, 2075–2085.
- (22) Lue, C. S.; Wong, S. F.; Huang, J. Y.; Hsieh, H. L.; Liao, H. Y.; Ramachandran, B.; Kuo, Y. K. *J. Appl. Phys.* **2013**, *113*, 013710.
- (23) Nam, G.; Jeon, J.; Kim, Y.; Kang, S. K.; Ahn, K.; You, T.-S. *J. Solid State Chem.* **2013**, *205*, 10–20.
- (24) Wang, P. L.; Kolodiazny, T.; Yao, J.; Mozharivskyj, Y. J. *Am. Chem. Soc.* **2012**, *134*, 1426–1429.
- (25) Zhao, H. J.; Ren, W.; Chen, X. M.; Bellaiche, L. J. *Phys.: Condens. Matter* **2013**, *25*, 385604.
- (26) Ishida, S.; Nakajima, M.; Liang, T.; Kihou, K.; Lee, C.-H.; Iyo, A.; Eisaki, H.; Kakeshita, T.; Tomioka, Y.; Ito, T.; Uchida, S.-i. *J. Am. Chem. Soc.* **2013**, *135*, 3158–3163.
- (27) Lehr, G. J.; Morelli, D. T.; Jin, H.; Heremans, J. P. *J. Appl. Phys.* **2013**, *114*, 223712.
- (28) Demirel, S.; Avci, S.; Altin, E.; Altin, S.; Yakinci, M. E. *Ceram. Int.* **2014**, *40*, S217–S222.
- (29) Fredrickson, D. C. *J. Am. Chem. Soc.* **2011**, *133*, 10070–10073.
- (30) Fredrickson, D. C. *J. Am. Chem. Soc.* **2012**, *134*, S991–S999.
- (31) Stacey, T. E.; Fredrickson, D. C. *Dalton Trans.* **2012**, *41*, 7801–7813.
- (32) Engelkemier, J.; Berns, V. M.; Fredrickson, D. C. *J. Chem. Theory Comput.* **2013**, *9*, 3170–3180.
- (33) Nielsen, O. H.; Martin, R. M. *Phys. Rev. B* **1985**, *32*, 3780–3791.
- (34) Godfrey, M. J. *Phys. Rev. B* **1988**, *37*, 10176–10183.
- (35) Ziesche, P.; Gräfenstein, J.; Nielsen, O. H. *Phys. Rev. B* **1988**, *37*, 8167–8178.
- (36) Filippetti, A.; Fiorentini, V. *Phys. Rev. B* **2000**, *61*, 8433–8442.
- (37) Treglia, G. In *Stress and strain in epitaxy; theoretical concepts, measurements, and applications*; Elsevier Science B.V.: Amsterdam, 2001; pp 119–150.
- (38) Rogers, C. L.; Rappe, A. M. *Phys. Rev. B* **2002**, *65*, 224117.
- (39) Hadler, A. B.; Harris, N. A.; Fredrickson, D. C. *J. Am. Chem. Soc.* **2013**, *135*, 17369–17378.
- (40) Berns, V. M.; Fredrickson, D. C. *Inorg. Chem.* **2013**, *52*, 12875–12877.
- (41) Fulfer, B. W.; McAlpin, J. D.; Engelkemier, J.; McCandless, G. T.; Prestigiacomo, J.; Stadler, S.; Fredrickson, D. C.; Chan, J. Y. *Chem. Mater.* **2014**, *26*, 1170–1179.
- (42) Hirshfeld, F. L. *Theor. Chim. Acta* **1977**, *44*, 129–138.
- (43) Buschow, K. H. J.; Van Der Goot, A. S.; Birkhan, J. J. *Less Common Met.* **1969**, *19*, 433–436.
- (44) Kleber, W. *Krist. Tech.* **1967**, *2*, 13–14.
- (45) Černý, R.; François, M.; Yvon, K.; Jaccard, D.; Walker, E.; Petricek, V.; Čisarová, I.; Nissen, H. U.; Wessicken, R. J. *Phys.: Condens. Matter* **1996**, *8*, 4485–4493.
- (46) Černý, R.; Guénée, L.; Wessicken, R. J. *Solid State Chem.* **2003**, *174*, 125–131.
- (47) Giovannini, M.; Pasero, R.; De Negri, S.; Saccone, A. *Intermetallics* **2008**, *16*, 399–405.
- (48) Gottlieb-Schönmeier, S.; Brühne, S.; Ritter, F.; Assmus, W.; Balanetsky, S.; Feuerbacher, M.; Weber, T.; Steurer, W. *Intermetallics* **2009**, *17*, 6–10.
- (49) Gonze, X.; Rignanese, G.-m.; Verstraete, M.; Beuken, J.-m.; Pouillon, Y.; Caracas, R.; Raty, J.-y.; Olevano, V.; Bruneval, F.; Reining, L.; Godby, R.; Onida, G.; Hamann, D. R.; Allan, D. C. *Z. Kristallogr.* **2005**, *220*, S58–S62.
- (50) Gonze, X.; Amadon, B.; Anglade, P.-M.; Beuken, J.-M.; Bottin, F.; Boulanger, P.; Bruneval, F.; Caliste, D.; Caracas, R.; Côté, M.; Deutsch, T.; Genovese, L.; Ghosez, P.; Giantomassi, M.; Goedecker, S.; Hamann, D. R.; Hermet, P.; Jollet, F.; Jomard, G.; Leroux, S.; Mancini, M.; Mazevet, S.; Oliveira, M. J. T.; Onida, G.; Pouillon, Y.; Rangel, T.; Rignanese, G.-M.; Sangalli, D.; Shaltaf, R.; Torrent, M.; Verstraete, M. J.; Zerah, G.; Zwanziger, J. W. *Comput. Phys. Commun.* **2009**, *180*, 2582–2615.
- (51) Goedecker, S.; Teter, M.; Hutter, J. *Phys. Rev. B* **1996**, *54*, 1703–1710.
- (52) Hartwigsen, C.; Goedecker, S.; Hutter, J. *Phys. Rev. B* **1998**, *58*, 3641–3662.
- (53) Momma, K.; Izumi, F. *J. Appl. Crystallogr.* **2011**, *44*, 1272–1276.
- (54) Oliveira, M. J. T.; Nogueira, F. *Comput. Phys. Commun.* **2008**, *178*, 524–534.
- (55) Okabe, A.; Sugihara, K.; Chiu, S. N. *Spatial tessellations: concepts and applications of Voronoi diagrams*, 2nd ed.; Wiley: Chichester, U.K., 2000; pp 43–52.
- (56) Bader, R. F. W. *Atoms in molecules: a quantum theory*; Oxford University Press: Oxford, England, 1990; pp 133–137.
- (57) Wood, E. A.; Compton, V. B. *Acta Crystallogr.* **1958**, *11*, 429–433.
- (58) Palenzona, A.; Manfrinetti, P. *J. Less Common Met.* **1982**, *85*, 307–312.
- (59) Greenwood, N.; Earnshaw, A. *Chemistry of the Elements*, 2nd ed.; Butterworth-Heinemann: Oxford, U.K., 1997; pp 111, 1148.
- (60) Bergerhoff, G.; Brown, I. D. In *Crystallographic Databases*; Allen, F. H., Bergerhoff, G., Sievers, R., Eds.; International Union of Crystallography: Chester, England, 1987; pp 77–95.
- (61) Belsky, A.; Hellenbrandt, M.; Karen, V. L.; Luksch, P. *Acta Crystallogr., Sect. B* **2002**, *58*, 364–369.
- (62) Pearson, W. B. *Acta Crystallogr., Sect. B* **1968**, *24*, 7–9.

- (63) Samson, S. *Nature* **1962**, *195*, 259–262.
- (64) Samson, S. *Acta Crystallogr.* **1965**, *220*, 401–413.
- (65) Samson, S. *Acta Crystallogr.* **1967**, *23*, 586–600.
- (66) Andersson, S. *Acta Crystallogr., Sect. B* **1980**, *36*, 2513–2516.
- (67) Cenzual, K.; Parthé, E.; Waterstrat, R. M. *Acta Crystallogr., Sect. C* **1986**, *42*, 261–266.
- (68) Yang, Q.-B.; Andersson, S.; Stenberg, L. *Acta Crystallogr., Sect. B* **1987**, *43*, 14–16.
- (69) Fredrickson, D. C.; Lee, S.; Hoffmann, R. *Angew. Chem., Int. Ed.* **2007**, *46*, 1958–1976.
- (70) Berns, V. M.; Stacey, T. E.; Sapiro, M.; Fredrickson, D. C. *Eur. J. Inorg. Chem.* **2011**, *2011*, 3936–3949.
- (71) Stacey, T. E.; Fredrickson, D. C. *Inorg. Chem.* **2013**, *52*, 8349–8359.
- (72) Henkelman, G.; Arnaldsson, A.; Jónsson, H. *Comput. Mater. Sci.* **2006**, *36*, 254–360.
- (73) Sanville, E.; Kenny, S. D.; Smith, R.; Henkelman, G. *J. Comput. Chem.* **2007**, *28*, 899–908.
- (74) Tang, W.; Sanville, E.; Henkelman, G. *J. Phys.: Condens. Matter* **2009**, *21*, 084204.
- (75) Raub, C. J.; Hamilton, D. C. *J. Less-Common Met.* **1964**, *6*, 486–488.
- (76) Haucke, W. *Z. Anorg. Allg. Chem.* **1940**, *244*, 17–22.
- (77) Dronskowski, R.; Blöchl, P. E. *J. Phys. Chem.* **1993**, *97*, 8617–8624.
- (78) Dwight, A. E. *Trans. Am. Soc. Met.* **1961**, *53*, 479–500.
- (79) Joseph, R. R.; Gschneidner, K. A., Jr. *Scr. Metall.* **1968**, *2*, 631–634.